AN INTEGRATED PORE-SCALE APPROACH FOR THE SIMULATION OF GRAIN MORPHOLOGY, WETTABILITY, AND SATURATION-HISTORY EFFECTS ON ELECTRICAL RESISTIVITY AND NMR MEASUREMENTS OF SATURATED ROCKS

Emmanuel Toumelin[1,2], Carlos Torres-Verdín[1], Sarath Devarajan[1], and Boqin Sun[3],
[1]The University of Texas at Austin   [2]Chevron USA   [3]Chevron Energy Technology Co.

ABSTRACT

NMR interpretation is usually based on models that neglect the presence of pendular rings and the different fluid distributions resulting from successive cycles of drainage and imbibition. We introduce a pore-scale approach that lends itself to the simulation of DC and NMR measurements in rocks saturated with two fluid phases that accounts for saturation history, wettability, and grain morphology effects. This approach is based on random walks and explicit tortuous fluid geometries formed by dense grain packings, fluid blobs, and wetting films. Fluids are distributed within the pore space following either pore-to-pore displacement or film-growth processes to reproduce drainage and imbibition cycles. Random-walk trajectories across these fluid volumes are used to simultaneously simulate electrical formation factor, resistivity index and NMR magnetization decay. Results emphasize the impact of rock morphology and saturation history on the variation of Archie's *n* saturation exponent. NMR magnetization decays are simulated for different echo times, thereby synthesizing parametric multidimensional NMR maps to identify fluid types, pore structure, and wettability. These simulations emphasize the impact of saturation history and oil viscosity on the interpretation of pore size, wettability, and fluid saturation from NMR measurements.

INTRODUCTION

Pore-scale modeling and simulation have become the preferred approach to quantify the influence of microscopic petrophysical properties on macroscopic correlations and mixing laws. Pore networks have been successful at reproducing multiphase-flow properties of porous rocks, even for the case of variable rock wettability. However, variable success and sometimes contradictory results have been obtained when simulating DC electrical conductivity in the presence of complex wettability and fluid geometries (Sallier and Hamon, 2005). Pore-network models usually discard the presence of intragranular porosity or clay exchange cations, which limits the range of rock morphologies that they can study. As in the case of electrical conductivity, conventional petrophysical NMR interpretation techniques (Kenyon, 1997) are based on simplified assumptions. First, fluid protons located within a given pore size are assumed to relax independently from protons located in surrounding pores. Strong pore heterogeneity or

diffusion coupling can substantially bias the estimation of pore size, irreducible fluids, and hydraulic permeability (Toumelin et al., 2003). Second, only one fluid is assumed to be present in each pore. It is now commonly understood that oil-wet (OW) pores remain water-wet (WW) in the least accessible pendular rings, thereby giving rise to mixed OW conditions and relaxation times that are difficult to predict from macroscopic NMR models. Finally, light fluids within isolated blobs or highly tortuous pathways experience restricted diffusion, which may affect NMR measurements. Recent developments in D/T_2 2D inversion of suites of NMR measurements have increased the accuracy of wettability, fluid saturation and fluid type determination (Sun and Dunn, 2002; Hürlimann et al., 2002). However, D/T_2 NMR map interpretation can also lead to ambiguous results in complex rock morphologies and fluid wettabilities (Toumelin et al., 2004). Therefore, pore-scale modeling seems an appropriate method to quantify the sensitivity of D/T_2 maps to a variety of pore-scale parameters, particularly the interplay between saturation history, wettability, fluid viscosity, and rock structure. To our knowledge, only a small number of results have been reported that integrate explicit pore-scale fluid descriptions with NMR simulations. In particular, Chang and Ioannidis (2001) based their work on pore network simulations where fluid phases totally filled the pores, thereby excluding mixed-OW pores. In similar fashion to our approach, Olayinka and Ioannidis (2002) used diffusion random walks to simulate the NMR response of stochastic rock replicas for single-phase saturation and neglecting the effects of magnetic field gradients in the pore space.

This paper introduces a pore-scale simulation method based on random walks and explicit object-oriented 3D grain and pore geometries that overcome some limitations of standard pore-scale simulation techniques. The method can be used to reproduce electrical conductivity and NMR rock responses for given rock structures and fluid viscosities, under the assumption of specific fluid flow processes. In the following sections, we summarize the numerical algorithm and describe simulation results for both DC conductivity and 2D NMR maps in WW and OW rocks.

SIMULATION MODEL
Random Walks for DC Electrical Conductivity and NMR
Particles within a fluid phase of free (bulk) diffusion coefficient D_{bulk} describe trajectories through iterative microscopic 3D displacements of length δr and duration δt such that

$$\delta r^2 = 6 D_{bulk} \; \delta t . \tag{1}$$

If **r** is the position vector of a walker in the pore space, and t is the walk time, the *effective* diffusivity of the fluid is related to the mean-square displacement over all walkers:

$$D(t) = \frac{\left\langle \left\| \mathbf{r}(t) - \mathbf{r}(0) \right\|^2 \right\rangle}{6t} . \tag{2}$$

Given the scale contrasts between the relevant length scales of rock and fluid (nm-thick films, sub-μm micropores, μm-scale pores, sub-mm grains, mm-scale vugs), we dynamically adjust the step size to be smaller than the smallest surrounding length scale.

We average such random trajectories until we obtain smooth $D(t)$ decay curves, with walk times long enough to reach asymptotic convergence within ±5% error. Figure 1 shows the time decay of effective water diffusivity computed in a 20% porosity (20 p.u.) tortuous pore space for different values of water saturation S_w.

From the equivalence between molecular diffusion and electrical conduction processes, the conductivity (σ) ratios F_R (formation factor) and I_R (resistivity index) are obtained from the diffusivity of brine across the brine-filled pore space (Clennell, 1997):

$$F_R = \frac{\sigma_{bulk}^{brine}}{\sigma_{S_w=100\%}^{sample}} = \frac{1}{\phi} \frac{D_{bulk}^{brine}}{D_{S_w=100\%}^{brine}(t \to \infty)}, \tag{3}$$

$$I_R = \frac{\sigma_{S_w=100\%}^{sample}}{\sigma_{S_w<100\%}^{sample}} = \frac{1}{S_w} \frac{D_{S_w=100\%}^{brine}(t \to \infty)}{D_{S_w<100\%}^{brine}(t \to \infty)}. \tag{4}$$

The NMR response of the synthetic medium is obtained by solving Bloch's equations along similar random-walk trajectories across each fluid-filled space (Toumelin et al., 2004). For CPGM acquisition sequences, one multiplies the magnetization amplitude M of a walker at the onset of each walk step by $\exp(-\delta t/T_2)$, where T_2 is given by the relation:

$$\frac{1}{T_2} = \frac{1}{T_{2bulk}} + \varepsilon \frac{\delta r}{3.84\rho} \quad . \tag{5}$$

In Eq. (5), T_{2bulk} is the bulk transverse relaxation time of the fluid, and ε is equal to 1 when the walker is located within one step of a relaxing surface of longitudinal relaxivity ρ, and 0 otherwise. The walker phase shift acquired during that step is calculated as

$$\delta\phi = \gamma B \delta t, \tag{6}$$

where γ is the proton gyromagnetic ratio and B is the background magnetic field amplitude exerted by the NMR magnet on the walker. If the walk clock coincides with a scheduled RF pulse, then the phase shift accumulated until then is reversed. If the clock coincides with a scheduled acquisition time t, then the recorded signal is equal to the mean of the projections $\left\langle M(t)\cos\left(\int_0^t \delta\phi\right)\right\rangle$ over the population of walkers. Suites of magnetization decays simulated for different echo times (Fig. 2) at various saturation levels are subsequently padded with 2-p.u. white noise and inverted with a 2D NMR inversion algorithm (Sun and Dunn, 2002) to synthesize parametric D/T_2 NMR maps.

Integrating Rock Morphology and Fluid Geometry through Pore and Grain Objects
The rock skeleton is formed by a disordered pack of overlapping spherical grains with intergranular pores. In order to define pore units and to maximize the efficiency of the random-walk algorithm, we partition the bulk volume into conforming tetrahedra using the Delaunay tessellation (Fig. 3). Each tetrahedron joins a set of four-closest grains centers and defines a pore unit in its void space, as well as 4 pore throats and 6 pendular rings. We consider grains as objects that are either solid or microporous. Microporous grains represent carbonate micrites or microporous cherts and are approximated with a consolidated cubic-centered packing of micrograins. In the presence of two fluid phases,

we define 3D pore objects following the sketches of Fig. 4. Within each partially-saturated pore, the volume occupied by hydrocarbon is delimited by a sphere centered on the pore space. The radius of that sphere is equal to the pore size R multiplied by a factor α_o. Continuity of the fluid phase from one pore to another is ensured when α_o is large enough and the oil phase in 2 neighboring pores reaches their delimiting throat. If the hydrocarbon blob does not wet the rock surface, then a water film of thickness T_w exists at the grain surface. Upon wettability alteration, an oil film of thickness T_o exists at the rock surface. Pendular rings of irreducible water develop at the intersection between the overlapping grains, where the fluid blob of radius $R.\alpha_o$ do not extend. This general pore geometry captures the canonical fluid configurations advanced by Kovscek et al.'s (1993) mixed-OW model. Random-walk trajectories of water particles are simultaneously defined across (a) the water-filled pore throats, (b) the wetting films, (c) the pendular rings, and (c) the microporous grains.

Fluid Distribution Model and Capillary-Pressure Hysteresis
The above fluid geometries are distributed within the Delaunay tessellation following two mechanisms of pore-to-pore piston-like propagation and film thickening, which alternate during 6 successive saturation cycles (Toumelin and Torres-Verdín, 2005). By convention, drainage here refers to the displacement of water by oil and imbibition refers to the opposite, regardless of wettability. For each piston-like displacement cycle, a pseudo capillary pressure (PCP) can be calculated and forms a series of hysteresis loops (Fig. 5).

- Cycle 1: drainage of the initially WW rock model through pore-to-pore oil propagation. Starting from the inlet face of the simulation domain (x=0 in Fig. 3), we assume oil blobs (as defined in pore type 2 of Fig. 4) progressively invade the pores on a neighbor-to-neighbor basis when two criteria are met: (i) the oil blob reaches the throat that separated the two pores, and (ii) the size of that throat is larger than a given threshold. Once the outlets faces other than x=0 are reached, the distribution of pore types 1 and 2 within the pore space defines the fluid geometry for the random walkers at a given water saturation. Drainage continues by decreasing the throat-size threshold (TST). At each saturation stage, PCP is calculated from the inverse of TST while water saturation is obtained by counting the proportion of randomly generated points in the water phase (section AB of Fig. 5a). Irreducible water saturation (reached at point B) is located in the pendular rings and the least accessible pores that cannot be reached by the $R.\alpha_o$-radius oil blobs. Before each subsequent cycle, TST is reset to a large value.

- Cycle 2: imbibition of the WW rock through pore-to-pore water propagation. Water is now injected from the inlet face x=0 (i.e., pores of type 2 revert back to type 1) and propagates from pore to pore when a new TST is met between two pores. The inverse of the imbibition TST is now subtracted from the PCP at the imbibition onset (point B) to yield new values of PCP for this cycle. This TST is decreased until S_w remains constant (point C). Irreducible oil saturation is located within type-2 pores trapped between type-1 pores. The hysteresis ABC of Fig. 5a agrees very well with the capillary-pressure hysteresis expected for a homogeneous rock.
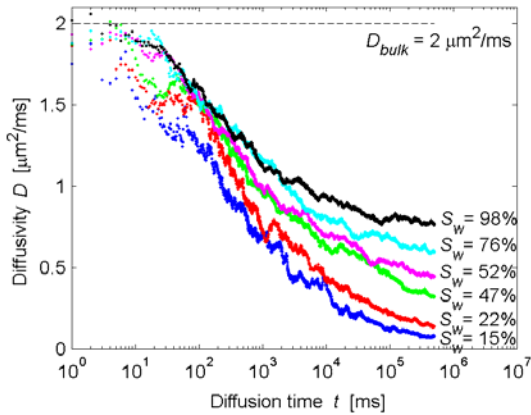
Figure 1. Examples of diffusivity time decays simulated for water molecules at different values of water saturation S_w, in a 20 p.u. tortuous pore space
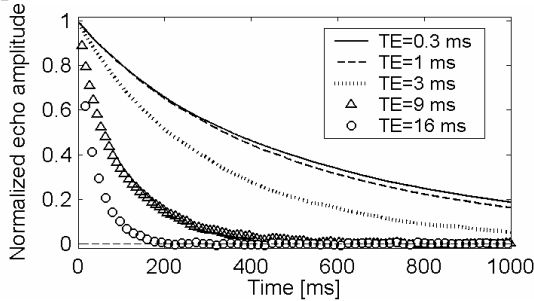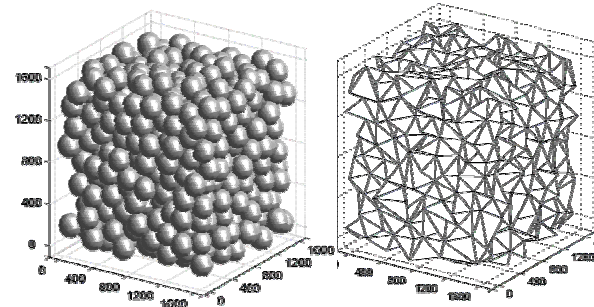

Figure 3. Example of a 1000-grain cubic subset from the Finney pack constructed with 100-μm grains (left), and corresponding Delaunay tessellation (right). All dimensions are given in μm

Figure 2. Examples of NMR magnetization time decays simulated in our rock model for different values of echo times
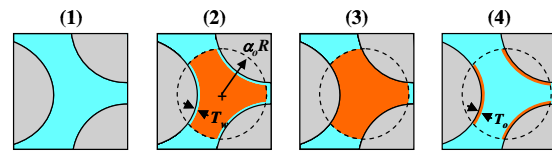

Figure 4. Illustration of the 4 pore types: (1) WW, water-saturated; (2) WW (water films of thickness T_w), invaded with hydrocarbons; (3) OW, hydrocarbon-saturated; (4) OW (oil films of thickness T_o), invaded with water
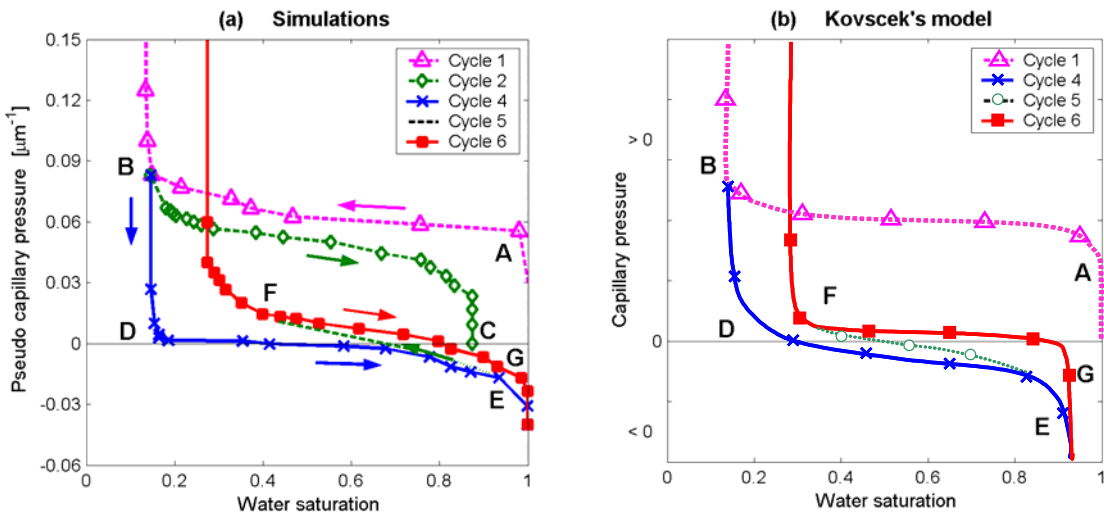

Figure 5. Comparison between (a) the pseudo-capillary pressure curves simulated with our 20-p.u. model and (b) the theoretical mixed-OW capillary pressure curves derived by Kovscek et al. (1993), for identical irreducible water saturations after Cycles 1 (13%) and 5 (23%)

- Cycle 3: imbibition of the WW rock through film thickening. This cycle is an alternate of Cycle 2 and models the fluid distribution resulting from the incremental growth of the wetting films (Kovscek et al., 1993). Starting from point B at 30 nm, the water films thicken and S_w increases accordingly. When the films become thick enough to fill pore throats, the NW phase is snapped-off and becomes isolated from the inlet; NW phase is now trapped and films stop thickening in those pores. Film growth is then iterated on the pores where NW phase remains connected to the inlet. Film thickness and PCP are not immediately related, so Cycle 3 is not represented on Fig. 5.
- Cycle 4: imbibition of the rock model after it underwent wettability alteration. All the type-2 pores are converted into type-3 pores, and then water is put in contact with the inlet. The process is similar to that of Cycle 1, except that pores change from type 3 to type 4 as water progresses in piston-like fashion across the pore space. The only criterion for water propagation across a pore throat is that its size meets a new TST. The PCP derived for this cycle is taken equal to the onset PCP (point B) minus the inverse of TST. In Fig. 5a, it describes the segment BDE and reaches PCP=0 at D. The endpoint E almost reaches S_w =100% because the only oil volume left in the rock is formed by the 30-nm thin films. OW pendular rings of oil would be required in the model to reach the curvature and the irreducible oil saturation of Fig. 5b.
- Cycle 5: drainage of the OW rock model. We only envisage the film-thickening mechanism to reproduce invasion of oil in the OW rock, after the model of Kovscek et al. (1993). This process is identical to WW Cycle 3. Likewise, no PCP is derived for this cycle. The segment EF represented in Fig. 5a only illustrates the transition between Cycles 4 and 6.
- Cycle 6: secondary imbibition of the OW rock model. This cycle starts from a configuration where most pores are filled with thick oil films and with water left at their center, disconnected from the inlet (point F in Fig. 5). Water is again put into contact with the inlet face and propagates pore by pore as long as a new TST is met, thus reconnecting the snapped-off water to the bulk water. The PCP for this cycle is just taken equal to the inverse of that TST (segment FG). Overall, The OW segments BDE and FG agree well with Kovscek et al.'s (1993) results (Fig. 5b), despite the absence of significant irreducible oil saturation in our model.

SIMULATION RESULTS IN WATER-WET ROCK MODELS
Formation Factor
We first used Eq. (3) to compute the formation factor of generic rock models. The solid grains in Finney's single-sized sphere pack (Bryant and Pallatt, 1996) were overgrown to reduce the pack porosity from 39 to 7 p.u. As shown in Fig. 6, random-walk (RW) results compared very well to those obtained using pore networks (PNs) and to published measurements in clay-free sandstones.

Resistivity Index Hysteresis (Saturation Cycles 1 to 3)
Figure 7 shows the resistivity index curve simulated as a function of S_w from Eq. (4) for drainage (Cycle 1). Archie's n saturation exponent appears as the negative slope of the

bilogarithmic plot. Simulation results agree well with measurements made on a 20-p.u. clay-free sandstone sample (core T1 from Argaud et al., 1989). Moreover, RW simulations yield a smoother resistivity index curve around $S_w=50\%$ than the PN simulations because the latter neglect presence of wetting films (Bryant and Pallatt, 1996). Figure 8 also shows
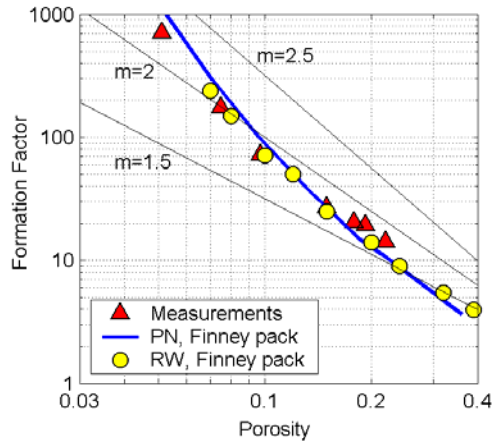

Figure 6. Comparison of formation-factor/ porosity crossplots measured in clay-free sandstones (Doyen, 1988) and simulated with pore networks (PN – Bryant and Pallatt, 1996) and random-walk (RW) techniques. Archie's lithology exponent *m* is equal to the negative slope of the bilogarithmic plot
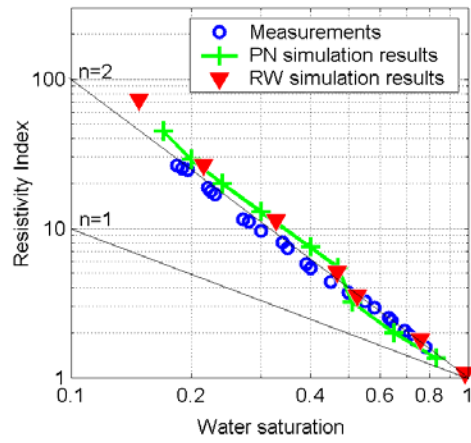
Figure 7. Comparison of primary-drainage resistivity-index curves measured in clay-free sandstone (core T1 from Argaud et al., 1989) and simulated with PN (neglecting thin-film conduction: Bryant and Pallatt, 1996) and RW techniques (allowing thin-film conduction: this work) with the 20-p.u. Finney pack
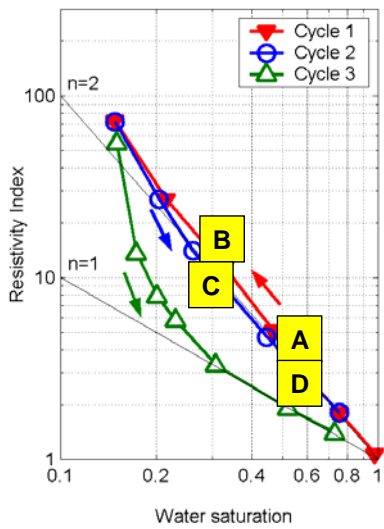
Figure 8. Resistivity index hystereses simulated during drainage and imbibition for a WW 20-p.u. Finney pack model (above) and evolution of D/T_2 NMR maps simulated along Cycles 1 and 2 with partial saturations of 1-cp oil grade (right)
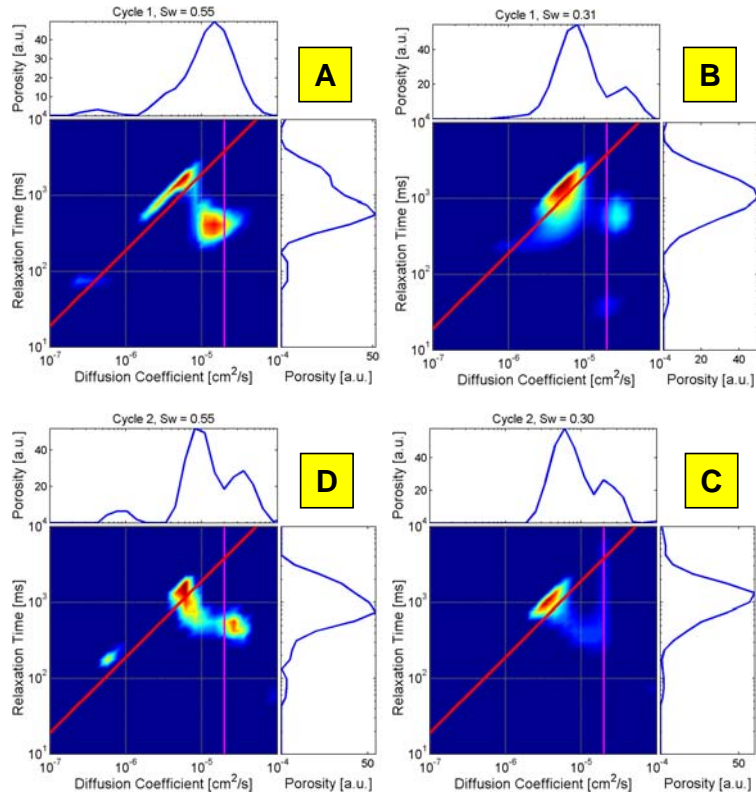
two distinct resistivity index hystereses calculated with the RW algorithm for drainage (Cycle 1) and each imbibition mechanism, pore-to-pore water invasion (Cycle 2) and incremental film growth (Cycle 3). The hysteresis consisting of Cycles 1 and 2 is hardly noticeable and n remains constant at 2.1. The other hysteresis formed by Cycles 1 and 3 exhibits values of n higher than 2 for S_w<25% and down to 1 for S_w>30%. The combination of both imbibition mechanisms in WW rocks could explain why measurements of n can be lower than 2.

Evolution of D/T_2 NMR Maps with Saturation History (Cycles 1 and 2)

Two-dimensional NMR maps capture the cross-distribution of fluid diffusivity and fluid T_2 relaxation time as bilogarithmic magnetization maps (Hürlimann et al., 2002). Peaks located along the diagonal line of the D/T_2 maps of Fig. 8 represent crude oil signal, while the peaks located along the vertical line at $D = 2.10^{-5}$ cm^2/s represent water signal. Figure 8 shows the D/T_2 2D NMR maps inverted from the NMR simulations performed in the 20-p.u. solid Finney pack, along Cycles 1 and 2, for discrete values of S_w. Echo-time values were equal to 0.3, 1, 3, 9 and 16 ms. The 2D maps are shown clockwise following the saturation history of the model for partial saturations of 1-cp oil ($D = 5.10^{-6}$ cm^2/s, $T_{2bulk} = 1$ s). At stage A, oil and water peaks are well defined and yield accurate fluid saturations and oil type. At subsequent stages, however, the proximity between the two fluid peaks biases the quality of the 2D inversion and interpretation errors ensue. For instance, the 2D NMR maps simulated at stages B and D underestimate S_w by at least 10 saturation units.

SIMULATION RESULTS IN OIL-WET ROCK MODELS

Influence of Porosity and Morphology on Resistivity Index (Cycles 1, 4, 5)

Figure 9a shows the resistivity index curves calculated along saturation Cycles 1, 4 and 5 for the 20-p.u. Finney pack. The WW and OW simulated hystereses replicate remarkably well the ones measured by Wei and Lile (1991), shown in Fig. 9b. They also emphasize the sudden increase of n as S_w decreases below a critical value S_{wcrit} during Cycle 5. The value of S_{wcrit} is the main difference between the simulation results of Fig. 9a (S_{wcrit}=40%) and the measurements reported in Fig. 9b (S_{wcrit}=55%). It is remarkable that rock porosity and morphology substantially influence the value of S_{wcrit}. Simulations performed on an overgrown 7-p.u. Finney pack constructed with solid grains exhibited a higher value of S_{wcrit}=60% (Fig. 9c). On the other hand, a 22-p.u. microporous pack constructed from a 14-p.u. overgrown Finney pack with 1/3rd solid grains and 2/3rd microporous grains yielded both a high value of irreducible water saturation (45%), a negative curvature of n for decreasing values of S_w, and a high value of S_{wcrit}= 72% (Fig. 9d). This last simulation case agrees very well with the resistivity-index measurements performed by Sweeney and Jennings (1960) on OW carbonates (Fig. 9e).

Evolution of D/T_2 NMR Maps with Saturation History (Cycles 1, 4-6)

We also synthesize D/T_2 NMR maps at discrete water saturations along Cycles 4 to 6 for the solid 20-p.u. Finney pack and for partial saturation of 1-cp oil. Figure 10 shows, clockwise, the resulting NMR intensity maps following the order of the stages labeled on the central panel of resistivity index. By contrast with the unimodal water response
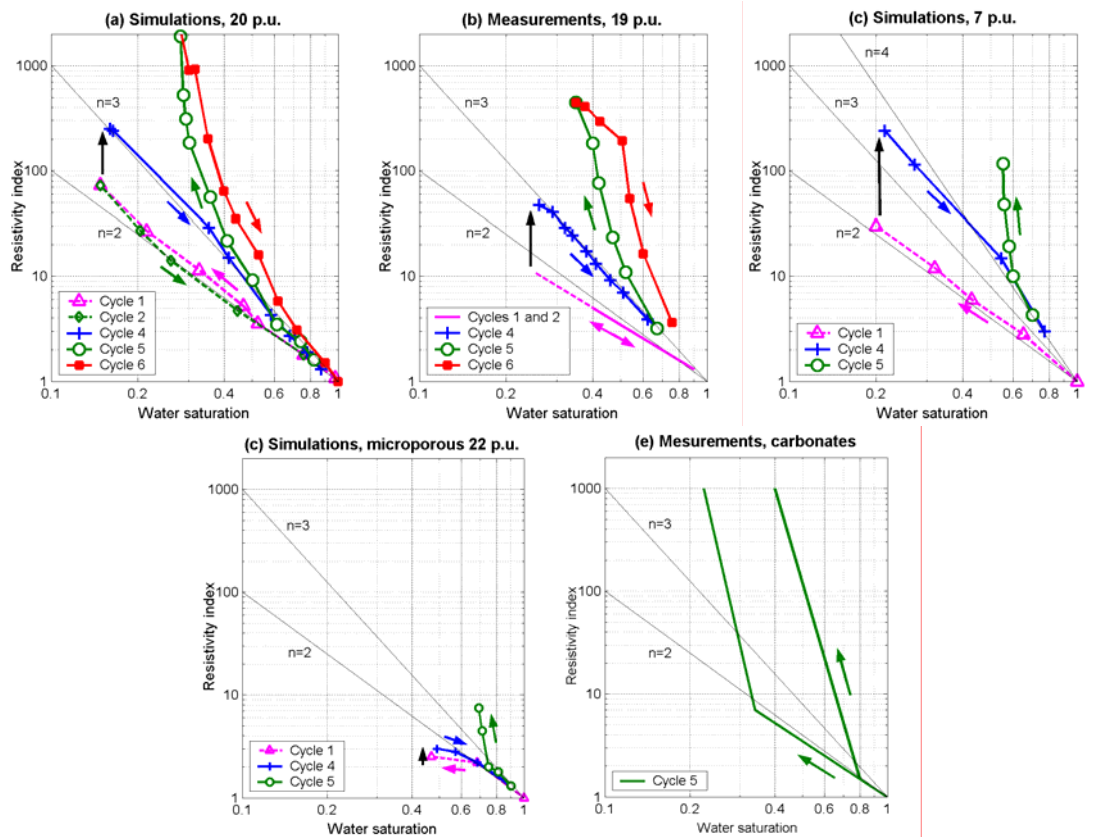
Figure 9. Comparison of resistivity-index curves: (a) simulated in 20-p.u. solid Finney pack; (b) measured in a 19-p.u. sandstone sample (Wei and Lile, 1991); (c) simulated in 7-p.u. solid Finney pack; (d) simulated in 22-p.u. microporous Finney pack; (e) measured in preserved OW carbonate samples (Sweeney and Jennings, 1960). Vertical arrows represent resistivity increases due to wettability alteration between Cycles 1 and 4

described in maps A and B, a distribution of relaxation times appears in subsequent NMR maps after wettability alteration. In maps C to E, a relaxation mode around T_2=3 s is always present corresponding to the response of water saturating OW regions of the pore space (in pores of type 4). Another mode appears at lower relaxation times representing the contribution of water that diffuses across the WW regions of the pore space. It is important to note that the T_2 value of that second mode varies along the saturation cycles as successive fluid invasion disconnects and reconnects the WW regions with the water-saturated pore volume. As S_w increases from stages C to D, water protons become decreasingly isolated inside pendular rings and increasingly connected to bulk pore space; therefore, values of relaxation time increase toward bulk relaxation. Simultaneously, the oil is light enough to be sensitive to oil/grain surface relaxation (the apparent oil peak T_2 value decreases from 1 s to 600 ms). For higher values of viscosity, surface relaxation does not affect the oil signal. During imbibition, wetting oil-films thicken and create divisions across the connected water-filled pore space. Consequently, part of the saturating water relaxes faster when S_w decreases. At stage E of Fig. 10, no snap-off has occurred yet and the water NMR peak extends continuously from T_2=800 ms to 3 s. At stage F, oil films become thick enough to promote snap-offs creating

boundaries between (a) water trapped in OW regions and exhibiting bulk relaxation time, and (b) water still connected between the center of the OW pores and the WW pendular rings. Similar simulations performed for higher values of oil grade (7 cp and above in ambient conditions) exhibited a marked bimodal water response at stage F and suggested that the NMR response was sensitive to this snap-off effect. However, for 1-cp oil saturation this bimodal water signal is confounded with the oil signal, which creates a large smeared peak in map F. The coincidence of oil and water D/T_2 peaks is frequent in the presence of 1-cp oil and adversely biases NMR interpretation results. In WW case B of Fig. 8, the water signal was already confounded with the light-oil signal, which was the main source of uncertainty in the assessment of S_w. Similar uncertainty arises for OW cases D to G described in Fig. 10. We note that the above variations of water T_2 distributions also affect estimates of irreducible saturations and hydraulic permeability, both being traditionally calculated from the T_2 distribution of water. Our simulations indicate errors in pore-size estimates of up to 300% in OW cases because of changing pore-level fluid configurations along saturation history. Using standard NMR permeability models in T_2^2 (Kenyon, 1997) would result in ten-fold errors in hydraulic permeability estimates.

CONCLUSIONS

We introduced a geometrical framework to simulate electrical conductivity and NMR rock responses with diffusion random walks. By applying simple drainage and imbibition heuristics, we obtained quantitative results supported by capillary pressure considerations and resistivity measurements. There is no doubt that the simulation method can be improved further with more accurate fluid displacement algorithms accounting for contact angle and grain curvature. Our simulations confirm the capacity of pore-scale models to capture the combined effect of saturation history, wettability and rock morphology on both rock electrical response and NMR. Specifically, we could quantitatively reproduce the influence of generic rock morphologies on OW Resistivity index hysteresis. The model helped identify that pore sizes and irreducible saturations in OW rocks could be mistakenly estimated from 2D NMR maps because of saturation history alone; we also identified configurations where wettability and fluid saturation could be incorrectly estimated because of lack of definition between the NMR responses of water and light oil. Another valuable application of such object-oriented grain pack geometry is to consider grains with clay coats where random walk steps are parameterized as a function of brine salinity (such as in Devarajan et al., 2006) to model the electrical response of shaly sands from pore-scale arguments.
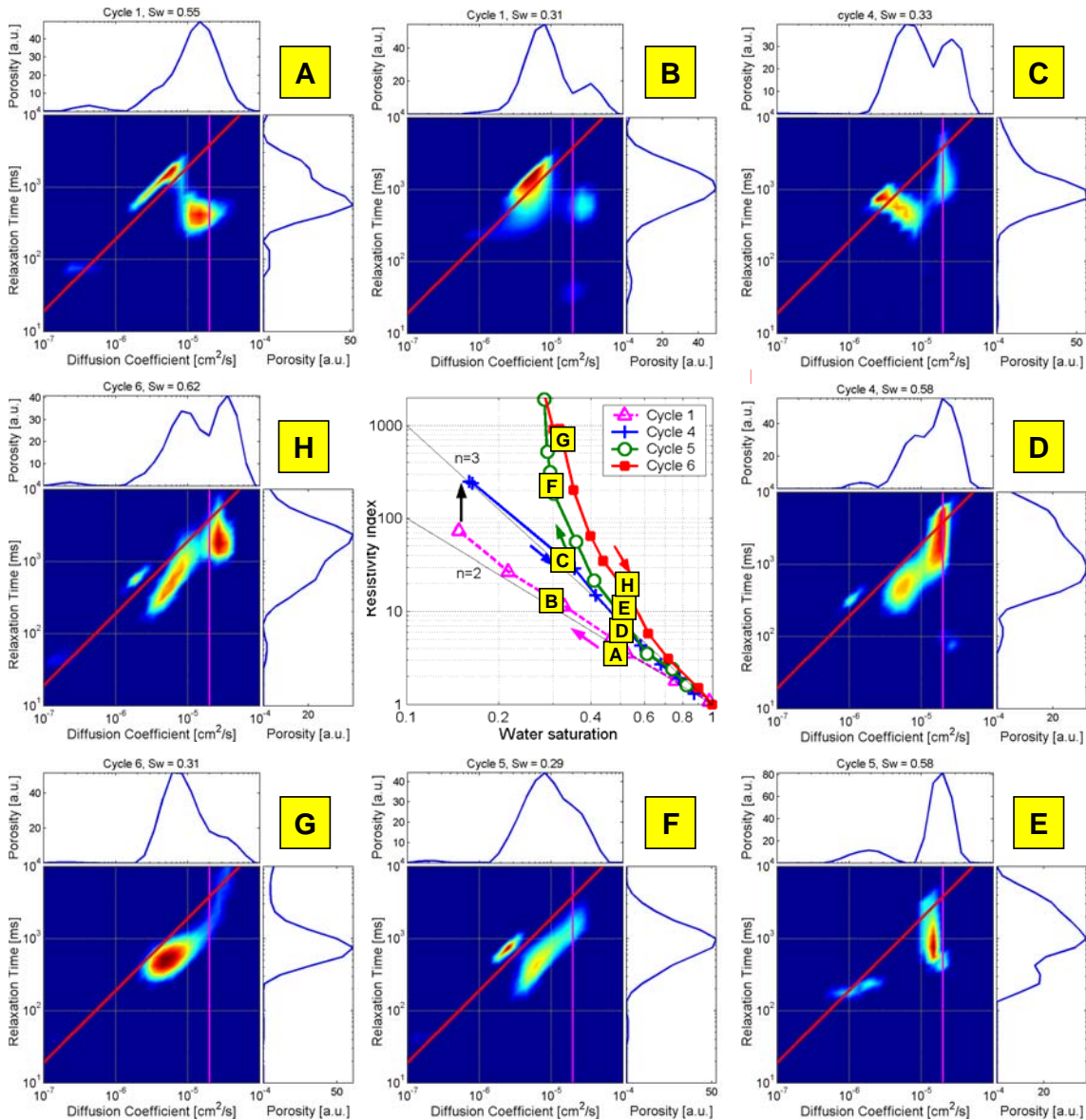
ACKNOWLEDGEMENTS

Figure 10. D/T_2 NMR maps simulated along Cycles 1, 4, 5 and 6 with partial saturations of 1-cp oil

REFERENCES

Argaud, M., H. Giouse, C. Straley, J. Tomanic, and K. Winkler, "Salinity and saturation effects on shaly sandstone conductivity" 1989 SPE ATCE paper 19577, San Antonio, Texas, 8-11 October.

Bryant, S., and N. Pallatt, "Predicting formation factor and resistivity index in simple sandstones," Journal of Petroleum Science and Engineering, (1996) **15**, 169-176.

Clennell, M.B., "Tortuosity: a guide through the maze," in Lovell, M.A, and Harvey, P.K. (eds.), Developments in Petrophysics, Geological Society Special Publication No. 122 (1997), 299-344.

Chang, D., and M.A. Ioannidis, "Pore network simulation of low-field NMR relaxometry under conditions of drainage and imbibition: effects of pore structure and saturation history," 2001 SCA International Symposium paper 18, Edinburgh, Scotland, 17-19 September.

Devarajan, S., E. Toumelin, C. Torres-Verdín, and E.C. Thomas, "Pore-scale analysis of the Waxman-Smits shaly sand conductivity model," 2006 SPWLA Annual Symposium, Vera Cruz, Mexico, 4-7 June.

Doyen, P., "Permeability, conductivity and pore geometry of sandstones," Journal of Geophysical Research, (1988) **93**, B7, 7729-7740.

Hürlimann, M., L. Venkataramanan, C. Flaum, P. Speier, C. Karmonik, R. Freedman and N. Heaton, "Diffusion-editing: new NMR measurements of saturation and pore geometry," 2002 SPWLA Annual Symposium paper FFF, Oiso, Japan, 2-5 June.

Kenyon, W.E., "Petrophysical Principles of Applications of NMR Logging," The Log Analyst, (1997) **38**, 2, 21-43.

Kovscek, A.R., H. Wong and C.J. Radke, "A pore-level scenario for the development of mixed wettability in oil reservoirs," AIChE Journal, (1993) **39**, 6, 1072-1085.

Olayinka, S., and M.A. Ioannidis, "Time-dependent diffusion and surface relaxation in reconstructed porous rock," 2002 SCA International Symposium paper 43, Monterey, California, 22-25 September.

Sallier, B., and G. Hamon, "Micritic milestone of the Middle East: Influence of wettability, pore network and experimental technique on drainage capillary pressure curve," 2005 SCA International Symposium paper 08, Toronto, Canada, 21-25 August.

Sun, B., and K.-J. Dunn, "Core Analysis with two dimensional NMR," 2002 SCA Symposium paper 38, Monterey, California, 22-25 September.

Sweeney, S.A., and H.Y. Jennings, "Effect of wettability on the electrical resistivity of carbonate rock from a petroleum reservoir," Journal of Physical Chemistry, (1960) **64**, 551-553.

Toumelin, E., and C. Torres-Verdín, "Influence of oil saturation and wettability on resistivity measurements: a uniform pore-scale approach," 2005 SPWLA Annual Symposium paper PPP, New Orleans, Louisiana, 26-29 June.

Toumelin, E., C. Torres-Verdín, S. Chen and D.M. Fischer, "Reconciling NMR measurements and numerical simulations: assessment of temperature and diffusive coupling effects on two-phase carbonate samples," Petrophysics, (2003) **44**, 2, 91-107.

Toumelin, E., C. Torres-Verdín, B. Sun, and K.-J., Dunn, "A numerical assessment of modern borehole NMR interpretation techniques," 2004 SPE ATCE paper 90539, Houston, Texas, 26-29 September.

Wei, J.-Z., and O.B. Lile, "Influence of wettability on two- and four-electrode resistivity measurements on Berea sandstone plugs," SPE Formation Evaluation, (1991) **6**, 4, 470-476.